2023 IEEE International Conference on Robotics and Automation (ICRA 2023)
May 29 - June 2, 2023. London, UK

CIOT: Constraint-Enhanced Inertial-Odometric Tracking for Articulated Dump Trucks in GNSS-Denied Mining Environments*

David Benz[1], Jonathan Weseloh[1], Dirk Abel[1], and Heike Vallery[1]

Abstract— **The ongoing electrification in all domains relies on strong increase in raw material extraction. Autonomous dump trucks are key to facilitating this. The automation requires the development of new localization approaches, as deep open-pit mines are challenging for satellite-based localization systems. Deep funnel-shaped mines reduce the sky-view angle from a certain position onward so that few to no satellites are visible. Therefore, we introduce a new wheel-odometry-aided navigation filter for articulated vehicles that fuses measurements from an inertial measurement unit (IMU), global navigation satellite systems (GNSS), and wheel encoders. Non-holonomic constraints are incorporated by assuming the lateral velocity of each wheel to be zero. We present two different measurement models that either use the wheel encoder signals of the rear wheels or all wheels of the articulated vehicle. This approach enables articulated vehicles to cope with the challenges of open-pit mines. The developed navigation filter is evaluated experimentally with an articulated dumper in two scenarios: A paved parking lot and a gravel pit. With the proposed method, we achieved a mean position error of $0.21\,\mathrm{m}$ during a $190\,\mathrm{s}$ test drive in the gravel pit with a simulated GNSS interruption of $90\,\mathrm{s}$. This is an improvement of $64\,\mathrm{m}$ compared to a state-of-the-art navigation filter that fuses only inertial and GNSS measurements.**

I. Introduction

Increasing electrification in all sectors is a major driver of demand for mineral raw materials. A key role will be played by the automation of mining vehicles, because autonomous transport units are expected to increase efficiency and operate more reliably in dangerous areas in mines.

For vehicle automation, accurate and robust vehicle localization is critical. The vehicle trajectory controller needs the position, velocity, and attitude at a high rate and without interruptions.

Traditional localization approaches fuse inertial measurements and GNSS signals (e.g., GPS) in a Kalman filter [1]. However, especially in deep open-pit mines, satellite-based localization methods might not be available everywhere. Therefore, further aiding sensors are required to maintain the robust vehicle state estimation.

Simultaneous Localization and Mapping (SLAM) is widely known [2], with its further development's lidar inertial odometry [3] and visual inertial odometry [4]. These methods combine localization and mapping in one algorithm. For example, in [5], a graph-based localization approach for autonomous construction robots is presented. This approach can handle GNSS interruptions by using a lidar sensor.

At first glance, these methods seem ideal, as the localization is robust against GNSS interruptions, and sufficient position accuracy is achieved in GNSS-denied environments. However, localization approaches based on optical sensors will fail due to dust and mud in rough mining terrains. Furthermore, large open-pit mines will result in insufficient key-point extraction and invalid data association in the field of view.

Wheel encoders, in contrast, do not rely on vision and can therefore also operate reliably in rough mining environments. Standard vehicle odometry combines wheel encoders, a gyroscope, and/or a steering angle sensor [6].

The measurement model to incorporate odometry information into a sensor fusion algorithm is often derived via the instantaneous center of rotation (ICR) of the vehicle [6]. This approach assumes that the vehicle is one rigid body. As this assumption does not hold for articulated vehicles, a new way to utilize vehicle kinematics has to be found. To our knowledge, only very limited work exists which uses odometry for localization of articulated vehicles. Either odometry is combined with visual perception of the environment [7], or wheel encoder information is completely disregarded [8], [9].

We propose to leverage additional information to achieve more reliable position estimates, namely mechanical constraints that are present in articulated vehicles. We unify the non-holonomic constraints with odometry and inertial sensing of the vehicle, leading to "constraint-enhanced inertial-odometric tracking" (CIOT). Whenever available, GNSS measurements are integrated to get absolute position and velocity information. In the following, we explain the algorithmic details of CIOT and investigate its precision and accuracy experimentally with an articulated truck. In the experiments, we also compare two versions of the algorithm, using two or four wheels, respectively.

The proposed navigation filter is a further development of previous filters developed in our research group. We have already shown in [1] and [10] that fusing inertial measurements with pseudo- and deltaranges from GPS and Galileo leads to a highly accurate state estimation. The benefits of GNSS integrity and differential corrections are shown in [11] and [12]. In [13], we evaluate a navigation filter for articulated vehicles utilizing odometry measurements from an optical speed sensor.

The remainder of this paper is structured as follows: Section II describes the navigation filter with the process

*This work was funded by the German Federal Ministry of Education and Research in the research project ARTUS (grant 033R126DN)

[1]D. Benz, J. Weseloh, D. Abel, and H. Vallery are with the Institute of Automatic Control, RWTH Aachen University, 52074 Aachen, Germany
d.benz@irt.rwth-aachen.de

model and the different measurement models. Section III describes the hardware setup and evaluation protocol. In Section IV, experimental results are presented and discussed. A conclusion and outlook are given in Section V.

II. Methods

A. Navigation Filter Overview

The tightly-coupled navigation filter is implemented according to [1] and estimates 18 states:

$$\boldsymbol{x} = [\boldsymbol{p}_{eb}^{e\,\mathrm{T}}\ \boldsymbol{v}_{eb}^{n\,\mathrm{T}}\ \boldsymbol{q}_{b}^{n\,\mathrm{T}}\ \boldsymbol{b}_{a}{}^{\mathrm{T}}\ \boldsymbol{b}_{g}{}^{\mathrm{T}}\ c_b\ c_d]^{\mathrm{T}}, \tag{1}$$

with the three-dimensional position of the body frame origin (b) with respect to the Earth-Centered-Earth-Fixed (ECEF) frame (e) $\boldsymbol{p}_{eb}^{e}$, the three-dimensional velocity of the body frame with respect to the ECEF frame in navigation frame (NED) coordinates (n) $\boldsymbol{v}_{eb}^{n}$, the quaternion representing the alignment of the body frame to the navigation frame $\boldsymbol{q}_{b}^{n}$, the biases of the accelerometer triad $\boldsymbol{b}_{\mathrm{a}}$, the biases of the gyroscope triad $\boldsymbol{b}_{\mathrm{g}}$, the GNSS receiver clock bias c_b, and the clock drift c_d. A schematic of the filter is depicted in Fig. 1.

A strapdown algorithm is used in the UKF prediction step to predict the state vector based on the measured acceleration $\tilde{\boldsymbol{f}}_{ib}^{b}$ and rotation rate $\boldsymbol{\omega}_{ib}^{b}$.

The position, velocity, and heading of the GNSS receiver is used to initialize the filter. Furthermore, the receiver provides pseudoranges and deltaranges of the main antenna.

Common-mode GNSS signal errors are corrected in a preprocessing step with pseudoranges of a reference station received via mobile communication. In the preprocessing of the odometry data, outliers are removed and the data is forwarded if the timestamp has incremented compared to the previous time step.

Depending on the received measurements in each time step, either the pseudorange (PR) and deltarange (DR) update and the odometry update are performed subsequently or only one of them is performed. In the following, the filter is explained in more detail.

B. Process Model

The navigation filter is implemented as an UKF. It uses a 6-DoF nonlinear discrete-time state-space model to estimate the states:

$$\boldsymbol{x}_{k+1} = \boldsymbol{f}_k(\boldsymbol{x}_k, \boldsymbol{u}_k)\Delta t + \boldsymbol{x}_k + \boldsymbol{G}_k \boldsymbol{w}_k, \tag{2}$$

where k denotes the time step of length Δt. The matrices $\boldsymbol{f}_k$ and $\boldsymbol{G}_k$ are defined as follows:

$$\boldsymbol{f}_k = \begin{pmatrix} \boldsymbol{C}_{n,k}^{e}\boldsymbol{v}_{eb,k}^{n} \\ \boldsymbol{C}_{b,k}^{n}(\tilde{\boldsymbol{f}}_{ib,k}^{b} - \boldsymbol{b}_{a,k}) - (2\boldsymbol{\omega}_{ie,k}^{n} + \boldsymbol{\omega}_{en,k}^{n}) \times \boldsymbol{v}_{eb,k}^{n} + \boldsymbol{g}_{\mathrm{l},k}^{n} \\ \boldsymbol{q}_{b,k}^{n} \otimes \Delta\boldsymbol{q}_k \\ \boldsymbol{0} \\ \boldsymbol{0} \\ c_{\mathrm{d},k} \\ 0 \end{pmatrix},$$

$$\boldsymbol{G}_k = \begin{pmatrix} \boldsymbol{0} & \boldsymbol{0} & \boldsymbol{0} & \boldsymbol{0} & \boldsymbol{0} & \boldsymbol{0} \\ \boldsymbol{C}_{b,k}^{n} & \boldsymbol{0} & \boldsymbol{0} & \boldsymbol{0} & \boldsymbol{0} & \boldsymbol{0} \\ \boldsymbol{0} & \boldsymbol{C}_{b,k}^{n} & \boldsymbol{0} & \boldsymbol{0} & \boldsymbol{0} & \boldsymbol{0} \\ \boldsymbol{0} & \boldsymbol{0} & \boldsymbol{I}_{3\times3} & \boldsymbol{0} & \boldsymbol{0} & \boldsymbol{0} \\ \boldsymbol{0} & \boldsymbol{0} & \boldsymbol{0} & \boldsymbol{I}_{3\times3} & \boldsymbol{0} & \boldsymbol{0} \\ \boldsymbol{0} & \boldsymbol{0} & \boldsymbol{0} & \boldsymbol{0} & 1 & 0 \\ \boldsymbol{0} & \boldsymbol{0} & \boldsymbol{0} & \boldsymbol{0} & 0 & 1 \end{pmatrix}$$

The position $\boldsymbol{p}_{eb}^{e}$, velocity $\boldsymbol{v}_{eb}^{n}$, and the quaternion $\boldsymbol{q}_{b}^{n}$ are propagated with the strapdown algorithm based on the measured acceleration $\tilde{\boldsymbol{f}}_{ib}^{b}$ and rotation rate $\boldsymbol{\omega}_{ib}^{b}$, according to [14].

The rotation matrices $\boldsymbol{C}_{n}^{b}$ and $\boldsymbol{C}_{n}^{e}$ rotate the corresponding vector from the NED to the body frame and from the NED to the ECEF frame, respectively.

Vectors $\boldsymbol{\omega}_{ie}^{n}$ and $\boldsymbol{\omega}_{en}^{n}$ are the Earth's rotation rate and the transport rate, respectively.

Gravity is compensated in the accelerometer measurements with the WELMEC model [15]. This model estimates the present gravitation $\boldsymbol{g}_{\mathrm{l}}^{n}$.

The new orientation results from a change in angle $\boldsymbol{\omega}_{nb,k}^{b}\Delta t$, represented here as the quaternion $\Delta\boldsymbol{q}$.

A random walk process is used to propagate the IMU biases $\boldsymbol{b}_{\mathrm{a}}$ and $\boldsymbol{b}_{\mathrm{g}}$, according to [16]. The receiver clock error c_{b} and drift c_{d} is modeled as a first-order Gauss-Markov process, according to [17]. The accelerometer noise $\boldsymbol{w}_{\mathrm{b_a}}$ and gyroscope noise $\boldsymbol{w}_{\mathrm{b_g}}$ are given in the body frame. The shape matrix $\boldsymbol{G}$ is therefore used to rotate the values into the navigation frame.

The propagation of the orientation is processed using orientation vectors within the filter, although the orientation is represented as a quaternion in the state vector. Therefore, $\boldsymbol{G}_{[3,2]}\boldsymbol{w}_{\mathrm{g}}$ corresponds only to a three-dimensional matrix, although the quaternion in the state vector is four-dimensional. For better comprehensibility, the conversion is omitted here.

C. Measurement Models

1) Odometry: Our research dumper has wheel encoders on each wheel and an articulation angle sensor. In the following, we present the odometry measurement model that calculates the wheel speed of each wheel in lateral and longitudinal direction. The measurement model is derived with the kinematic vehicle model, depicted in Fig. 2.

We made two simplifying assumptions: First, we neglected scale factor errors, which would summarize uncertainties in the wheel radii [18]. These uncertainties occur due to tire wear or a change of the load, the temperature, or the pressure. Second, we assume that the effect of wheel slip is negligible at low speeds. We use this assumption to incorporate nonholonomic constraints into our measurement model.

The navigation filter estimates the velocity in NED frame. To derive the wheel speeds, the velocity has to be rotated into the vehicle rear body frame, which coincides with the IMU frame:

$$\boldsymbol{v}_{\mathrm{IMU}} = \boldsymbol{C}_{n}^{b}\boldsymbol{v}_{eb}^{n}. \tag{3}$$

The velocities of the rear wheels can be calculated as the sum of the IMU velocity and the current lever arm effect

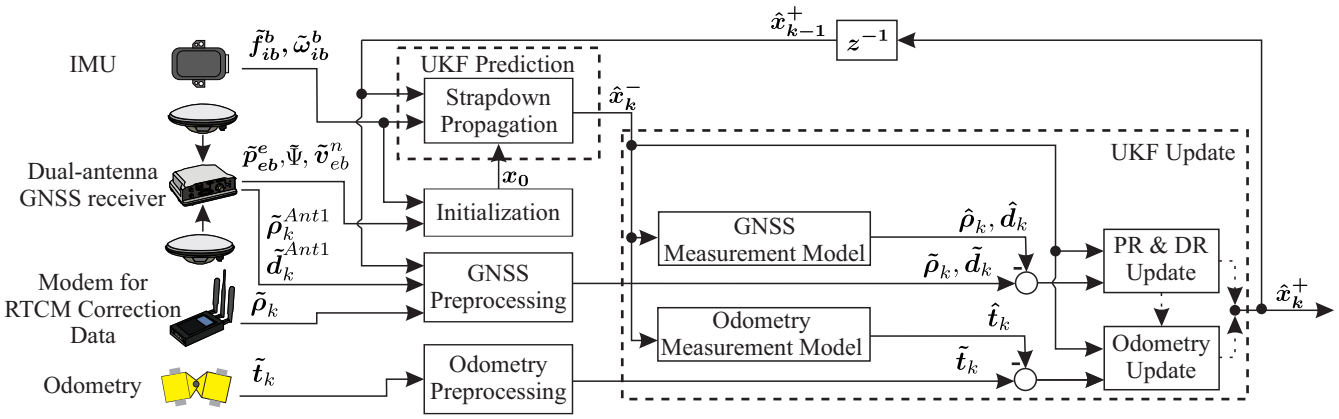

Fig. 1: Navigation filter with sequential measurement models. The pseudorange (PR) and deltarange (DR) update is performed before the Odometry update, if GNSS and Odometry measurements are available. The corresponding update step is skipped if either of the measurements is unavailable. The state vector and covariance matrix are updated in the update blocks according to the UKF theory.

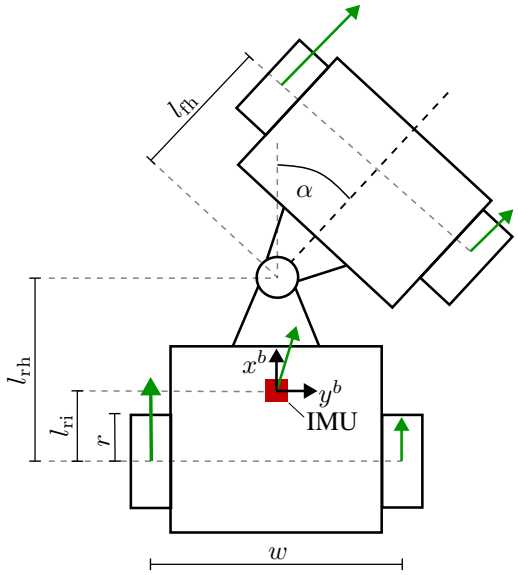

Fig. 2: Schematic depiction of the articulated dumper. The green arrows represent the speed at the respective points.

caused by rotation. For example, the velocity of the right (r) rear (r) wheel is

$$\boldsymbol{v}_{\mathrm{rr}} = \boldsymbol{v}_{\mathrm{IMU}} + (\boldsymbol{\omega}^b_{ib} - \boldsymbol{b}_g) \times \begin{pmatrix} -l_{\mathrm{ri}} \\ w/2 \\ 0 \end{pmatrix}. \tag{4}$$

Similarly, the hinge velocity $\boldsymbol{v}_{\mathrm{Hinge}}$ is:

$$\boldsymbol{v}_{\mathrm{Hinge}} = \boldsymbol{v}_{\mathrm{IMU}} + (\boldsymbol{\omega}^b_{ib} - \boldsymbol{b}_g) \times \begin{pmatrix} l_{\mathrm{rh}} - l_{\mathrm{ri}} \\ 0 \\ 0 \end{pmatrix}. \tag{5}$$

To calculate the velocities of the front wheels, the angular velocity of the vehicle front body is needed. As there is no IMU mounted on the front body, the angular velocity is approximated from the sum of the z-axis rotation rate of the rear body and the steering angle rate $\dot{\alpha}$:

$$\boldsymbol{\omega}_{\mathrm{f}} = \begin{pmatrix} 0 \\ 0 \\ (\omega^{ib}_{b,3} - b_{\mathrm{g},3}) + \dot{\alpha} \end{pmatrix}. \tag{6}$$

The front wheel velocities subsequently result from the velocity of the hinge and the front body's angular velocity. The velocity of the front (f) right (r) wheel, for example, is:

$$\boldsymbol{v}_{\mathrm{fr}} = \boldsymbol{v}_{\mathrm{Hinge}} + \boldsymbol{\omega}_{\mathrm{f}} \times \begin{pmatrix} \cos(\alpha) l_{\mathrm{fh}} - \sin(\alpha) w/2 \\ \sin(\alpha) l_{\mathrm{fh}} + \cos(\alpha) w/2 \\ 0 \end{pmatrix}. \tag{7}$$

Rotating the velocity vector by the steering angle provides its lateral and longitudinal components:

$$\begin{pmatrix} v_{\mathrm{fr,long}} \\ v_{\mathrm{fr,lat}} \\ \dots \end{pmatrix} = \boldsymbol{v}^{\mathrm{T}}_{\mathrm{fr}} \begin{pmatrix} \cos(\alpha) & -\sin(\alpha) & 0 \\ \sin(\alpha) & \cos(\alpha) & 0 \\ 0 & 0 & 1 \end{pmatrix}. \tag{8}$$

The wheel speeds of the left wheels result analogously.

The wheel encoders deliver the measurement vector $\tilde{\boldsymbol{z}} = \begin{pmatrix} \tilde{v}_{\mathrm{fl}} & \tilde{v}_{\mathrm{fr}} & \tilde{v}_{\mathrm{rl}} & \tilde{v}_{\mathrm{rr}} \end{pmatrix}$. Non-holonomic constraints are integrated into the measurement model through pseudomeasurements of the lateral wheel speeds with value zero:

$$\tilde{\boldsymbol{z}} = (\underbrace{\tilde{v}_{\mathrm{fl}} \quad \tilde{v}_{\mathrm{fr}} \quad \tilde{v}_{\mathrm{rl}} \quad \tilde{v}_{\mathrm{rr}}}_{\text{longitudinal}} \quad \underbrace{0 \quad 0 \quad 0 \quad 0}_{\text{lateral}}) \tag{9}$$

2) GNSS: Pseudoranges and Deltaranges of GPS and Galileo received with a single antenna are processed in the navigation filter. Before using the GNSS data, an integrity check is applied according to [11], and differential corrections are performed using pseudoranges from a reference station ([12]). The GNSS measurement models for the pseudorange ρ^i_k and deltarange d^i_k of the i-th satellite are according to [12]:

$$\underbrace{\begin{pmatrix} \rho^i_k \\ d^i_k \end{pmatrix}}_{\boldsymbol{z}_k} = \underbrace{\begin{pmatrix} \|\boldsymbol{p}^{e,i}_{es,k} - \boldsymbol{p}^e_{ea,k}\| + c_{\mathrm{b},k} \\ (\boldsymbol{e}^{e,i}_{as,k})^{\top} (\boldsymbol{v}^{e,i}_{es,k} - \boldsymbol{v}^e_{ea,k}) + c_{\mathrm{d},k} \end{pmatrix}}_{\boldsymbol{h}_k(\boldsymbol{x})} + \begin{pmatrix} \nu^i_{\rho,k} \\ \nu^i_{\mathrm{d},k} \end{pmatrix}, \tag{10}$$

with the normalized direction vector from the antenna to the i-th satellite $\boldsymbol{e}_{as,k}^{e,i}$, the clock error c_b, the clock drift c_d, the measurement noise of the pseudorange and deltarange ν_ρ^i and ν_d^i, respectively, the known position of each satellite $\boldsymbol{p}_{es}^{e,i}$, and the position of the main antenna derived from the estimated position of the body frame and the lever arm between body frame and main antenna:

$$\boldsymbol{p}_{ea,k}^{e} = \boldsymbol{p}_{eb,k}^{e} + \boldsymbol{C}_{n,k}^{e}\boldsymbol{C}_{b,k}^{n}\boldsymbol{l}_{ba}^{b}. \tag{11}$$

$\boldsymbol{v}_{es}^{e,i}$ is the velocity of the i-th satellite and $\boldsymbol{v}_{ea}^{e}$ is the velocity of the main antenna:

$$\boldsymbol{v}_{ea,k}^{e} = \boldsymbol{C}_{n,k}^{e}\left(\boldsymbol{v}_{eb,k}^{n} + \boldsymbol{C}_{b,k}^{n}(\boldsymbol{\omega}_{eb,k}^{b} \times \boldsymbol{l}_{ba}^{b})\right). \tag{12}$$

3) Optical Speed Sensor: To validate the wheel odometry measurement models, a high-precision optical speed sensor is used as reference odometry. Using an optical sensor as reference has the benefits of measuring the slip-free velocity over ground. The sensor used is the Kistler Correvit S-Motion DTI. The sensor points on the ground and measures the slip-free two-dimensional speed over ground with a distance resolution of $<1\,\mathrm{mm}$. The measurement model is according to [13], but simplified by neglecting the sensor misalignment compensation. It estimates the two-dimensional speed $\boldsymbol{v}_{es,k}^{s}$ of the sensor frame s relative to the ECEF frame e given in the sensor frame:

$$\underbrace{\boldsymbol{v}_{es,k}^{s}}_{\boldsymbol{z}_k} = \underbrace{\boldsymbol{C}_{b}^{s}(\boldsymbol{C}_{n,k}^{b}\boldsymbol{v}_{eb,k}^{n} + \boldsymbol{\omega}_{ib,k}^{b} \times \boldsymbol{l}_{bs}^{b})}_{\boldsymbol{h}_k(\boldsymbol{x})} + \boldsymbol{\nu}_{s,k}. \tag{13}$$

$\boldsymbol{C}_{n}^{b}$ rotates the velocity from the state vector given in the NED frame to the IMU body frame b. The effect of the lever arm between the IMU body frame and the sensor frame $\boldsymbol{l}_{bs}^{b}$ is compensated with $\boldsymbol{\omega}_{ib}^{b} \times \boldsymbol{l}_{bs}^{b}$, where, $\boldsymbol{\omega}_{ib}^{b}$ describes measured rotations around the IMU body frame. The rotation matrix $\boldsymbol{C}_{b}^{s}$ rotates the estimated velocity, finally, as the sensor y-axis and the IMU body frame y-axis point in opposite directions. $\boldsymbol{\nu}_\mathrm{s}$ is the measurement noise.

D. Initialization and Parametrization

The initial position, velocity, heading, clock bias, and drift are determined with the GNSS receiver. The initial roll and pitch angles are determined with the accelerometer.

The gyroscope biases are initialized by averaging the measurements over five seconds. Due to vehicle vibrations, the initial accelerometer biases are set to zero.

The UKF covariance matrices $\boldsymbol{Q}_0$, $\boldsymbol{R}_{\mathrm{GNSS},0}$ and $\boldsymbol{P}_0$ are initialized as described in [17]. The determination of the covariance matrix of the Correvit is explained in [13]. The measurement covariance matrix of the odometry is only occupied on the main diagonal. The longitudinal and lateral components are weighted differently, with four equal values each. The values are determined with a batch simulation for every evaluation scenario. Thereby, the parametrization which results in the lowest mean position error is chosen. This is done to get the best filter performance and to demonstrate the capability of the odometry measurement model. Online parameter estimation for cross-scenario performance should be targeted in the future.

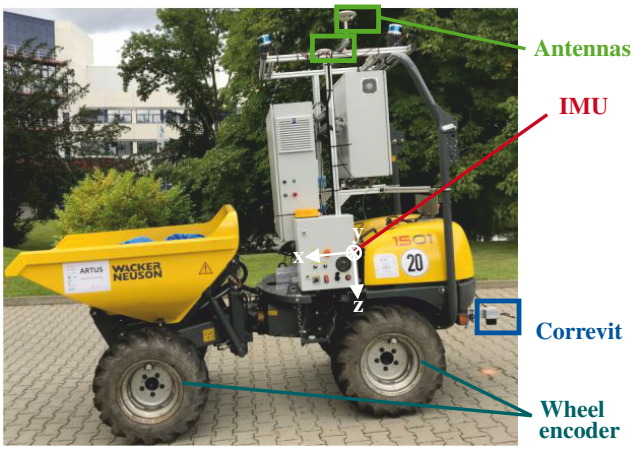

Fig. 3: Research dumper from the project ARTUS. All sensors except the wheel encoders are placed on the rear vehicle body.

III. Experimental Evaluation

A. Hardware Setup

In this work, the proposed approach is tested with the small articulated dumper shown in Fig. 3. The vehicle speed was limited to around $5\,\mathrm{km/h}$ during manual operation with a remote control. This limit was set because a delay in the actuators of almost $1\,\mathrm{s}$ makes manual driving very unintuitive.

All measurement equipment was mounted on the vehicle's rear body. A LORD MicroStrain 3DM-Gx5-25 IMU and a Novatel PwrPak7 dual-antenna GNSS receiver combined with two survey antennas are used. The navigation filter uses only measurements from one antenna. The second antenna is used for the internal receiver solution, which is used for initializing the filter and as ground truth.

All wheels were equipped with a wheel encoder and a reluctor wheel with 100 teeth. The optical speed sensor (Kistler S-Motion DTI) provided the two-dimensional speed over ground.

All sensor data was logged on a real-time industrial computer.

B. Evaluation Protocol

Four navigation filters are evaluated, which differ only in the measurement models used. Table I gives an overview of the filters. CIOT is evaluated with two configurations: One uses all wheel measurements and the other only the measurements of the rear wheels.

TABLE I: Filter configurations for evaluation.

Filter Name	Configuration
Standard	IMU + GNSS
Correvit	IMU + GNSS + Correvit odometry
CIOT 2-Wheel	IMU + GNSS + 2-Wheel odometry
CIOT 4-Wheel	IMU + GNSS + 4-Wheel odometry

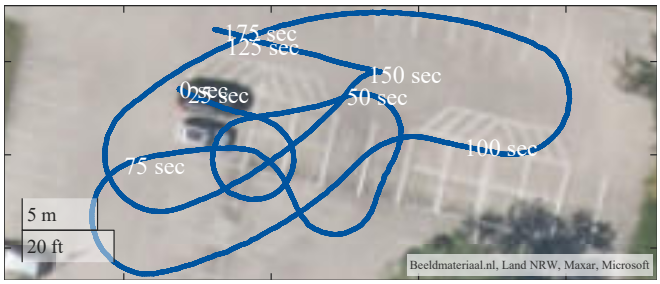

(a)

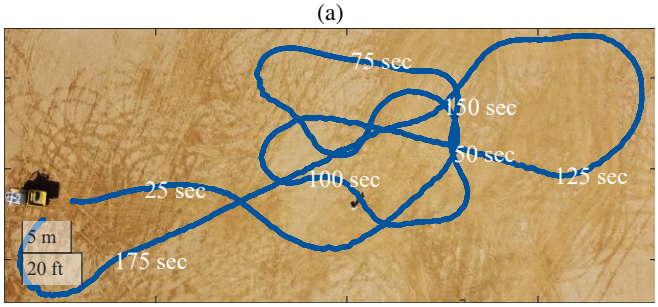

(b)

Fig. 4: Birds-eye view of the driven trajectories. Tests were conducted in a parking lot a) and in a gravel pit b). The data belongs to the GNSS receiver's reference solution. The timestamps correspond to those of all other evaluation figures. Image credit for a): Maxar, Microsoft.

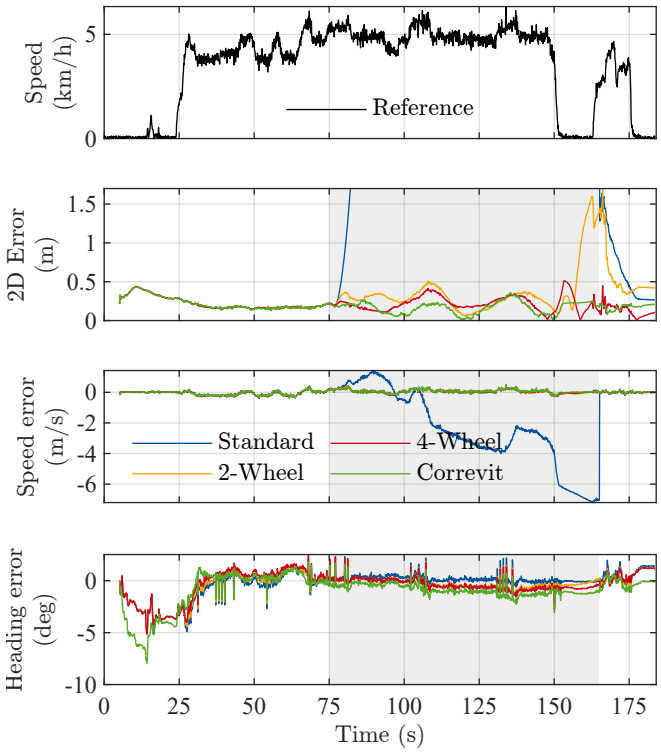

Fig. 5: Evaluation plots of the test drive in the parking lot. The gray area indicates the simulated GNSS interruption.

Two different scenarios are used to evaluate filter performance. Fig. 4 shows the driven trajectories in birds-eye view. The first test site is a parking lot with a paved surface, and the second is a gravel pit. The gravel pit consists of loose sandy soil with many potholes. During the test drive, the vehicle had a payload of about $200\,\mathrm{kg}$.

To validate the filter performance in GNSS-denied environments, GNSS outages are simulated by blocking all GNSS signals as both test sites had perfect GNSS conditions.

C. Performance Measures

For later use in real production operations with dump trucks, the localization should achieve certain accuracies. Since mines can be very extensive, we assume a position error of $0.5\,\mathrm{m}$ and a heading error of $3°$ as acceptable.

The odometry-aided filters are compared to the Correvit-aided filter, which uses a high-accuracy optical speed sensor and, therefore, serves as a reference odometry approach. The GNSS receiver's position, speed, and heading in RTK-fix mode serve as ground truth. The 2D position error is calculated as the Euclidean distance between the filter and the receiver position. Important error values for both test drives are summarized in Table II.

IV. Results and Discussion

A. Parking Lot

Fig. 5 shows different evaluation plots of the test drive. The vehicle speed is shown in the upper plot. The small peaks in the beginning result from a steering motion at standstill. After driving for about $125\,\mathrm{s}$ at an almost constant speed, the dumper stopped, waited, and reversed.

The 2D position error, the speed error, and the heading error is depicted in the lower plots of 5.

In the first $75\,\mathrm{s}$, GNSS is available; therefore, the position error is at about $0.2\,\mathrm{m}$ for all filters. GNSS is then turned off for the next $90\,\mathrm{s}$. After turning GNSS off, indicated with the gray area, the Correvit filter remains converged with a mean position error of $0.19\,\mathrm{m}$. The standard filter drifts away as expected immediately after turning off GNSS. Four-wheel CIOT achieves a mean position error of $0.21\,\mathrm{m}$ and is not affected by the standstill and reversing. Two-wheel CIOT diverges during standstill, resulting in a maximum position error of $1.6\,\mathrm{m}$. Directly after reversing, the position estimation converges again, resulting in a total mean position error of $0.26\,\mathrm{m}$.

Even though all filters estimate different positions, the velocity is estimated with no major differences except for the standard filter.

The estimated heading converges quickly after the start for all filters. The mean heading errors for the standard filter, the Correvit-aided filter, two-wheel, and four-wheel CIOT all remain below our predefined limit of $3°$, with $0.75°$, $0.81°$, $0.91°$, and $1.31°$, respectively. The standard filter achieves the best heading result.

The small spikes in the heading errors result from missing reference data for some timesteps.

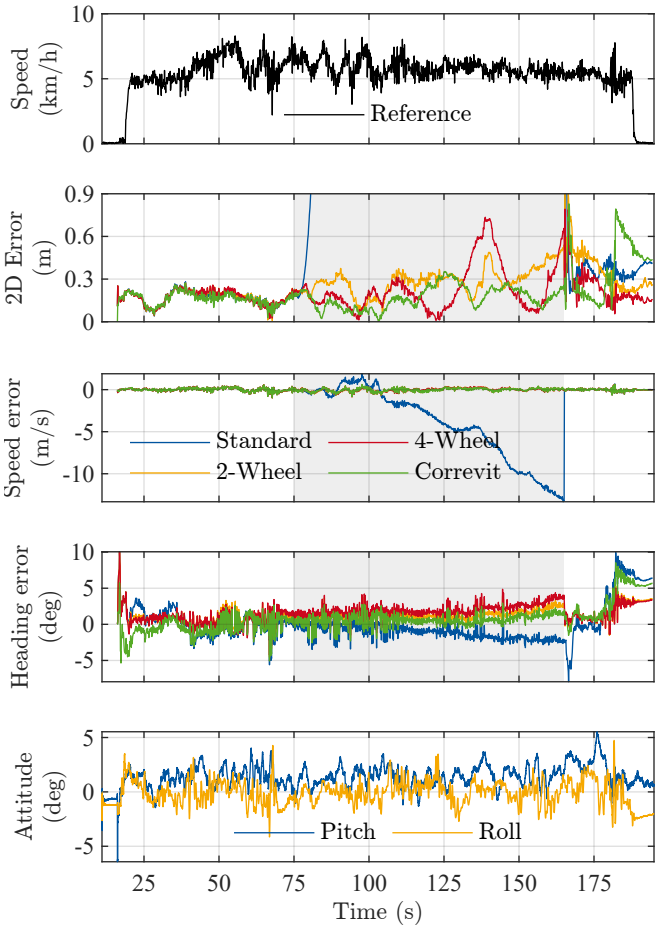

Fig. 6: Evaluation plots of the test drive in the gravel pit. The gray area indicates the simulated GNSS interruption.

B. Gravel Pit

Fig. 6 shows the evaluation plots. A GNSS interruption of 90 s was simulated after 75 s. The speed was again almost constant at about $5\,\mathrm{km\,h^{-1}}$.

Again, the mean position error was at about 0.2 m for the first 75 s for all filters. During the period without GNSS signals, the estimated position of both odometry filters remains converged, except for a short period after 125 s. An abrupt movement of the vehicle, reflected in a roll movement followed by a pitch movement, deteriorates the estimated position for a short time. A deep pothole after about 180 s affects the CIOT filters less than the other filters, while GNSS is available again. This applies to the position error as well as to the heading error.

All filters estimate the velocity again with no major differences; only the standard filter diverges as expected.

The vehicle vibrations due to uneven ground result in a noisy reference heading and, therefore, noisy heading errors. The harsh environment is demanding for the odometry approach. Nevertheless, the heading error can be kept below 5° with both CIOT approaches during the period without GNSS. The mean heading error is slightly larger than during the experiment on the parking lot, with 1.37° and 1.67° for 2-wheel and 4-wheel CIOT, respectively.

TABLE II: Position and heading errors of the four offline evaluated filters for all presented experiments ($\overline{x}$: mean value, σ: standard deviation).

Filter	2D-error (m) $\overline{x}$	2D-error (m) σ	Heading error (°) $\overline{x}$	Heading error (°) σ
Parking lot				
Standard	54.16	85.48	0.75	1.03
CIOT 2-Wheel	0.32	0.26	0.81	0.98
CIOT 4-Wheel	0.21	0.09	0.91	0.93
Correvit	0.19	0.09	1.31	1.34
Gravel pit (approx. 200kg payload)				
Standard	64.19	115.96	1.75	1.82
CIOT 2-Wheel	0.26	0.11	1.37	0.97
CIOT 4-Wheel	0.21	0.13	1.67	1.05
Correvit UKF	0.20	0.13	1.33	1.49

C. Comparison to Requirements

The mean error values for the proposed CIOT filters for both test drives are below the maximum permissible position error of 0.5 m and heading error of 3° assumed for autonomous dump trucks. Nevertheless, the limits are sometimes exceeded for a short time.

D. Limitations and Future Work

In this work, we optimally parameterized the odometry measurement covariance matrix based on a batch simulation, using the same data as for evaluation. In the future, we want to evaluate the filter using additional, longer datasets, and also investigate online adaptive estimation of these parameters, to ensure good cross-scenario performance.

There are several possibilities to further increase the performance of the proposed filter:

Different variances for the front wheels should be considered, as the measurement model uncertainty is larger for these wheels due to the measurement noise of the steering angle and incomplete knowledge on the angular velocity of the front body.

Alternatively, better results of the four-wheel model can also be expected by using a second IMU to measure the currently unknown rotation rates of the vehicle front body.

In addition, at standstill, drifting of the position can be prevented by a zero-velocity update.

V. Conclusion

In this paper, we showed how our proposed constraint-enhanced inertial-odometric tracking (CIOT) of articulated vehicles can deliver accurate and precise tracking in GPS-denied mining environments. This allows autonomous mining vehicles to navigate through areas where GNSS reception is limited or unavailable. Wheel encoders are inexpensive, allowing mass integration of this localization system. To verify that the proposed method is suitable for much harsher environments, longer experiments should be conducted in a funnel-shaped mine with real GNSS outages.

REFERENCES

[1] T. Konrad, J.-J. Gehrt, J. Lin, R. Zweigel, and D. Abel, "Advanced state estimation for navigation of automated vehicles," *Annual Reviews in Control*, vol. 46, pp. 181–195, 2018.

[2] S. Thrun, W. Burgard, and D. Fox, *Probabilistic Robotics*. MIT Press, Aug. 2005.

[3] T. Shan, B. Englot, D. Meyers, W. Wang, C. Ratti, and D. Rus, "LIO-SAM: Tightly-coupled Lidar Inertial Odometry via Smoothing and Mapping," in *2020 IEEE/RSJ International Conference on Intelligent Robots and Systems (IROS)*, Oct. 2020, pp. 5135–5142.

[4] S. Cao, X. Lu, and S. Shen, "GVINS: Tightly Coupled GNSS–Visual–Inertial Fusion for Smooth and Consistent State Estimation," *IEEE Transactions on Robotics*, vol. 38, no. 4, pp. 2004–2021, Aug. 2022.

[5] J. Nubert, S. Khattak, and M. Hutter, "Graph-based Multi-sensor Fusion for Consistent Localization of Autonomous Construction Robots," in *2022 International Conference on Robotics and Automation (ICRA)*, May 2022, pp. 10 048–10 054.

[6] B. Liu, M. Adams, and J. Ibanez-Guzman, "Multi-aided Inertial Navigation for Ground Vehicles in Outdoor Uneven Environments," in *Proceedings of the 2005 IEEE International Conference on Robotics and Automation*, Apr. 2005, pp. 4703–4708.

[7] Z. Dang, T. Wang, and F. Pang, "Tightly-coupled Data Fusion of VINS and Odometer Based on Wheel Slip Estimation," in *2018 IEEE International Conference on Robotics and Biomimetics (ROBIO)*, Dec. 2018, pp. 1613–1619.

[8] S. Scheding, G. Dissanayake, E. Nebot, and H. Durrant-Whyte, "An experiment in autonomous navigation of an underground mining vehicle," *IEEE Transactions on Robotics and Automation*, vol. 15, no. 1, pp. 85–95, 1999.

[9] H. Mäkelä, "Overview of LHD navigation without artificial beacons," *Robotics and Autonomous Systems*, vol. 36, no. 1, pp. 21–35, Jul. 2001.

[10] J.-J. Gehrt, T. Konrad, J. Lin, M. Breuer, D. Abel, and R. Zweigel, "High Precision Localisation with Dual-Constellation for Railway Applications," in *Proceedings of the International Technical Meeting of The Institute of Navigation*, Reston, Virginia, 2018, pp. 35–45.

[11] S. Liu, J.-J. Gehrt, D. Abel, and R. Zweigel, "Dual-Constellation Aided High Integrity and High Accuracy Navigation Filter for Maritime Applications," in *Proceedings of the 2019 International Technical Meeting of The Institute of Navigation*, Reston, Virginia, 2019, pp. 762–774.

[12] M. Nitsch, J.-J. Gehrt, R. Zweigel, and D. Abel, "Tightly Coupled INS/GNSS Navigation Filter for the Automation of a River Ferry," *IFAC-PapersOnLine*, vol. 54, no. 16, pp. 139–145, Jan. 2021.

[13] D. Benz, J.-J. Gehrt, R. Zweigel, and D. Abel, "Speed Sensor-Aided Navigation Filter for Robust Localization in GNSS-Denied Mining Environments," in *Proceedings of the 2022 International Technical Meeting of The Institute of Navigation*, 2022, pp. 1457–1468.

[14] J. Wendel, *Integrierte Navigationssysteme: Sensordatenfusion, GPS und Inertiale Navigation*, 2nd ed. Oldenbourg Wissenschaftsverlag, 2011.

[15] Welmec, "Guide on Common application of Directive 2009/23/EC Non-automatic weighing instruments," 2015.

[16] M. G. Petovello, "Real-time integration of a tactical-grade IMU and GPS for high-accuracy positioning and navigation," Ph.D. dissertation, University of Calgary, 2003.

[17] M. Breuer, T. Konrad, and D. Abel, "High Precision Localisation in Customised GNSS Receiver for Railway Applications," in *29th International Technical Meeting of The Satellite Division of the Institute of Navigation*, Portland, Oregon, 2016, pp. 779–787.

[18] P. Groves, *Principles of GNSS, Inertial, and Multisensor Integrated Navigation Systems*, 2nd ed. Artech House, 2013.